

Journal of Medical Imaging

MedicalImaging.SPIEDigitalLibrary.org

Model-based beamforming with plane wave synthesis in medical ultrasound

Kazuyuki Dei
Jaime Tierney
Brett Byram

SPIE•

Kazuyuki Dei, Jaime Tierney, Brett Byram, "Model-based beamforming with plane wave synthesis in medical ultrasound," *J. Med. Imag.* 5(2), 027001 (2018), doi: 10.1117/1.JMI.5.2.027001.

Model-based beamforming with plane wave synthesis in medical ultrasound

Kazuyuki Dei,* Jaime Tierney, and Brett Byram

Vanderbilt University, Department of Biomedical Engineering, Nashville, Tennessee, United States

Abstract. We are interested in examining how our model-based beamforming algorithm, referred to as aperture-domain model image reconstruction (ADMIRE), performs on plane wave sequences in conjunction with synthetic aperture beamforming. We also aim to identify the impact of ADMIRE applied before and after synthetic focusing. We employed simulated phantoms using Field II and tissue-mimicking phantoms to evaluate ADMIRE as applied to synthetic sequencing. We generated plane wave images with and without synthetic aperture focusing (SAF) and measured contrast and contrast-to-noise ratio (CNR). For simulated cyst images formed from single plane waves, the contrast for delay-and-sum (DAS) and ADMIRE are 15.64 and 28.34 dB, respectively, whereas the CNR are 1.76 and 3.90 dB, respectively. We also applied ADMIRE to simulated resolution phantoms having a point target at 3 cm depth on-axis. We simulated the point spread functions from data obtained from 1 plane wave and 75 steered plane waves, along with linear scans with 3 and 4 cm- focal depths. We then compared the outcome of applying ADMIRE before and after SAF using 3 and 11 steered plane waves. Finally, we applied this to an *in vivo* carotid artery. Based on the findings in this study, ADMIRE can be adapted to full field insonification sequences to improve image quality in plane wave imaging. Additionally, we investigated how robustly ADMIRE performs in the presence of random noise. We then address identified limitations using a conventional envelope detection method with decluttered signals. © 2018 Society of Photo-Optical Instrumentation Engineers (SPIE) [DOI: 10.1117/1.JMI.5.2.027001]

Keywords: medical ultrasound; beamforming; clutter suppression; plane wave imaging; synthetic aperture focusing; model; random noise; envelope detection; speckle statistics.

Paper 17322PR received Oct. 25, 2017; accepted for publication Apr. 2, 2018; published online Apr. 26, 2018.

1 Introduction

Today's modern ultrasound platforms can provide high quality images *in vivo*. However, imaging artifacts still impair the effectiveness of ultrasound in medicine. To minimize such artifacts, numerous beamformers have been introduced.¹⁻⁴ Aperture domain model image reconstruction (ADMIRE) is one such beamformer that uses a physical model of aperture domain signals, developed by our group.^{5,6}

In previous studies, we demonstrated that ADMIRE has the ability to suppress reverberation artifacts, off-axis clutter, and wavefront aberration from *in vivo* B-mode data.^{6,7} ADMIRE also addresses limitations of related beamforming methods because it preserves post-processed channel signals and preserves speckle texture and statistics of normal B-mode. Additionally, the clutter reduction does not impact resolution as other traditional clutter suppression methods like apodization do.⁸ Based on these findings, we have established that ADMIRE is an effective tool to reduce artifacts in ultrasound images.

We previously used conventionally focused beam sequences and concentrated on reducing imaging artifacts caused by reverberation. However, because ADMIRE also showed robustness to suppress off-axis clutter, we were interested in how ADMIRE performs on images obtained from unfocused beams used to insonify a broad field of view. As reported in the literature, unfocused beam sequences provide lower resolution and lower contrast images compared with focused beams, due to transmit beam broadening.⁹ We hypothesize that ADMIRE may be

useful to restore image degradation resulting from broad field insonification.

Two common types of waves that allow a single transmit beam to acquire an entire field of view are plane waves and diverging waves.^{10,11} Plane wave sequences have been used in medical ultrasound to obtain higher frame rates, compared with conventional focused beam sequences, especially when imaging nonstationary objects (e.g., dynamic elastography and blood flow imaging¹²). Given the recent interest in using unfocused, full field insonification sequences for high-speed imaging, we explored ADMIRE's potential to suppress clutter resulting from plane wave sequences.¹³ To compensate for loss of image quality while maintaining high frame rates, these sequences often involve the acquisition of plane waves at multiple angles that are then coherently summed to synthesize continuous transmit focusing, a method that we have not evaluated in conjunction with ADMIRE.

The objective of this study is to evaluate the performance of ADMIRE in conjunction with plane wave transmit sequencing and synthetic aperture focusing (SAF) using simulation, phantom, and *in vivo* data. Because ADMIRE is a nonlinear processing method, we also examine the effect of applying ADMIRE either before or after SAF on 3 and 11 steered plane waves. We also demonstrate the impact of random noise on the ADMIRE model decomposition and reconstruction. Finally, we identified some limitations of using a conventional software envelope detection method so we demonstrate the benefits of an alternative envelope detector.

*Address all correspondence to: Kazuyuki Dei, E-mail: kazuyuki.dei@vanderbilt.edu

2 Methods

2.1 Simulated and Experimental Data

To conduct this study, we utilized both contrast and resolution phantom data obtained using single and multiple steered plane waves. The base phantom datasets were prepared and distributed for the Plane-wave Imaging Challenge in Medical UltraSound (PICMUS), which was a competitive event using common data, independently organized during the 2016 IEEE International Ultrasonic Symposium.^{14,15} The dataset consists of two sets of phantom data used for evaluating ADMIRE, including (1) simulated phantoms generated using Field II simulation,^{16,17} and (2) tissue-mimicking phantom data acquired using a Verasonics ultrasound system (Verasonics Inc., Kirkland, WA, USA) with a linear array transducer (L11-4v). Field II simulation details are indicated in Table 1, whereas Table 2 identifies parameters used to acquire RF channel data on the Verasonics platform.

2.2 ADMIRE Algorithm and Parameters

The ADMIRE algorithm models the received wavefronts at the surface of the transducer aperture, which we call the aperture domain. ADMIRE accounts for the spherical wavefronts, short-time Fourier Transform (STFT), pulse-bandwidth correction, and angular sensitivity.⁶ The model equation can be analytically expressed in the following form:

$$p_s(x; t, \omega) = \sum_{n=0}^{N-1} A_n(x) e^{j\omega\tau(x; x_n, z_n, \tau_n)}, \quad (1)$$

where p_s is the scattered pressure, x is the aperture position, t and ω are the time and frequency to identify the localized signal, $\tau(x; x_n, z_n, \tau_n)$ is the wavefront delay for a received echo signal scattering from point (x_n, z_n) at time delay τ_n , and N is the number of scatterers arriving at time t , respectively. $A_n(x)$ is the lateral amplitude weighting across the transducer from element sensitivity,¹⁸ also incorporating the axial STFT window effects, the reflected pulse shape, and the exact wavefront delay profile of $\tau(x; x_n, z_n, \tau_n)$.⁶

Table 1 Field II simulation parameters.

Parameters	Values
Number of elements	128
Width of elements	0.27 mm
Height of elements	5.00 mm
Pitch	0.30 mm
Aperture length	38.4 mm
Center frequency (f_c)	5.208 MHz
Sampling frequency (f_s)	20.832 MHz
Bandwidth	35%
Transmitted pulse	2.5 cycles
f -number	1.75

Table 2 L11-4v linear probe setting.

Parameters	Values
Number of elements	128
Width of elements	0.27 mm
Height of elements	5.00 mm
Pitch	0.30 mm
Aperture length	38.4 mm
Center frequency (f_c)	5.208 MHz
Sampling frequency (f_s)	20.832 MHz
Bandwidth	35%
Transmitted voltage	30 V
Transmitted pulse	2.5 cycles
f -number	1.75

In the implementation of ADMIRE, a design matrix of model predictors is constructed using the physical model in Eq. (1), while we apply the Fourier transform (FT) to delayed channel signals at a small range of depths to convert into the frequency domain, as follows:

$$s_i(mT) \xrightarrow{\mathcal{F}} S_i(mT, \omega_p), \quad (2)$$

where i is the indices channel element, mT is the discrete time index, T is the sampling time period of the channel data, ω_p is a discrete frequency, $s_i(mT)$ is delayed channel signal for channel element i at the discrete time mT , $S_i(mT, \omega_p)$ is the FT signal for a single channel of the aperture i , and $\xrightarrow{\mathcal{F}}$ is the FT operator, respectively. We then express a single frequency of the aperture domain signal at a given depth, denoted as y , in the following linear model:

$$y = X\beta, \quad (3)$$

where X is the ADMIRE design matrix (i.e., the matrix of predictors) corresponding to a given depth and frequency and constructed from the physical model in Eq. (1), and β is the coefficient vector for the predictors in X . y , X , and β are initially complex: $y \in \mathbb{C}^{\mathbb{N} \times 1}$, $X \in \mathbb{C}^{\mathbb{N} \times \mathbb{M}}$, $\beta \in \mathbb{C}^{\mathbb{M} \times 1}$, where \mathbb{N} is twice of the number of aperture elements and \mathbb{M} is the total number of model predictors, but most efficient solvers only allow real inputs (e.g., code by Friedman et al.¹⁹), so y and X are then expressed with the following matrices, decomposing complex signals into real (\Re) and imaginary (\Im) components, respectively,

$$y = [\Re\{S_i(mT, \omega_p)\} \Im\{S_i(mT, \omega_p)\}]^T, \quad (4)$$

$$X = \begin{bmatrix} \Re\{p_s(x; t, \omega)\}^T & -\Im\{p_s(x; t, \omega)\}^T \\ \Im\{p_s(x; t, \omega)\}^T & \Re\{p_s(x; t, \omega)\}^T \end{bmatrix}, \quad (5)$$

where T denotes the nonconjugate matrix transpose. The β vector is also adjusted accordingly.

The solution of the linear model in Eq. (3) is illposed. To solve the illposed inverse problem in Eq. (3), we perform model decomposition (i.e., model-fitting) using elastic-net regularization that linearly combines L1 and L2 penalties,²⁰ given by

$$\hat{\beta} = \min_{\beta} \{ \|y - X\beta\|^2 + \lambda[\alpha\|\beta\|_1 + (1 - \alpha)\|\beta\|_2^2/2] \}, \quad (6)$$

where $\|\beta\|_1$ and $\|\beta\|_2$ denote the L1 and L2 norms, respectively, and α and λ terms control the degree and type of regularization. For example, the parameter of α ranges between 0 and 1 to adjust the relative weight of L1 and L2, whereas the degrees of freedom (df) is a function of λ , as addressed by Tibshirani et al.²¹

Because the model decomposition process in ADMIRE reproduces a given wavefront using model predictors, we can identify the spatial location of the decomposed signal within the field of view. Based on the information, we select only energy inside the region of interest (ROI) and remove scatterers outside this region. In short, model predictors from within the acceptance zone are reconstructed to reproduce the signal of interest while rejecting other model predictors. We refer to the reconstructed signals as decluttered signals, given in the following form:

$$y_{\text{SOI}} = X_{\text{ROI}}\hat{\beta}_{\text{ROI}}, \quad (7)$$

where y_{SOI} is a decluttered signal, X_{ROI} is the model with predictors that are spatially within the acceptance zone that is accounted for in the ROI, and $\hat{\beta}_{\text{ROI}}$ is the corresponding model coefficients. When implementing ADMIRE, the acceptance zone is specified as an ellipse, based on the expected lateral and axial resolutions⁶ of res_{lat} and res_{axl} , respectively, given by

$$\left(\frac{x_n - x_r}{c_{\text{lat}}\text{res}_{\text{lat}}} \right)^2 + \left(\frac{z_n - z_r}{c_{\text{axl}}\text{res}_{\text{axl}}} \right)^2 \leq 1, \quad (8)$$

where x_r and z_r denote the center of the acceptance zone, and c_{lat} and c_{axl} are scalable factors for the acceptance region laterally and axially, respectively. The post-ADMIRE decluttered signals in Eq. (7) are converted back into the time-domain using the inverse short-time Fourier Transform (ISTFT).²²

When applying the ADMIRE algorithm to a specific transmit beam sequencing, two major factors substantially impact performance. One is the spatial sampling of the predictors used to create X in Eq. (3), whereas the other is the elastic-net regularization parameters (α and λ) in Eq. (6). In our previous *in vivo* study using ADMIRE, the model space was finely sampled within the acceptance zone and coarsely sampled outside the region (i.e., the rejection zone) for all depths shallow to the acceptance zone, to effectively suppress reverberation artifacts. However, assuming that reverberation will not be a substantial source of degradation in this study, ADMIRE was implemented with the model space confined to the depth around the acceptance zone, allowing the algorithm to focus on off-axis clutter reduction. In this study, we tuned the model space sampling and regularization parameters specifically for each number of summed plane waves. Unless stated, we apply synthetic plane wave focusing before applying ADMIRE.²³ Table 3 indicates ADMIRE parameters used in this study.

Synthetic focusing is the process whereby the received signals of individual aperture elements are synthetically focused and used to reconstruct images.²⁴⁻²⁶ When using this method, a transmitted pulse can insonify an entire field of interest and

Table 3 ADMIRE parameters.

Parameter	Value
α	0.9
λ	Tunable variable
c_{lat}	6
c_{axl}	2
Model space (lateral) [m]	Aperture length
Model space (axial) [m]	$z_r \pm (c_{\text{axl}}\text{res}_{\text{axl}})/2$
Model sampling (inside) [m]	$\{0.0716\text{res}_{\text{lat}}, 0.286\text{res}_{\text{axl}}\}$
Model sampling (outside) [m]	$\{1.43\text{res}_{\text{lat}}, 1.43\text{res}_{\text{axl}}\}$
STFT window size	$[8 \log(2)]/(2\pi\text{BW}f_c)$

Note: BW is the fractional bandwidth and f_c is the center frequency of transmitted pulse.

the received signals from each transmit pulse are collected and processed to form a B-mode image that is typically a low-resolution image. The resulting sets of low resolution data are coherently summed, providing a high-resolution image with dynamic transmit focusing throughout the field of view. The resulting images, after summing data from each steered plane wave image, have high resolution and high contrast compared with a single plane wave image.

2.3 ADMIRE Computational Complexity

Compared with delay-and-sum (DAS) beamforming, ADMIRE has additional steps to implement, including the STFT operation, model decomposition, reconstruction, and the inverse-STFT as described previously. These all increase the computational complexity. First, a computational order of $\mathcal{O}(pqr \log q)$ is introduced for the STFT operation, where p is the number of channels, q is the number of samples in each short-time window, and r is the total number of windows through depth, respectively. Next, model decomposition with an elastic-net regularization technique has a computational cost of $\mathcal{O}(u^3 + u^2v)$, where u is the number of model predictors actually used in the fit and v is the total number of model predictors in the ADMIRE design matrix X in Eq. (5).^{6,20} This has to be done for every depth and frequency. A computational order of reconstruction is $\mathcal{O}(u)$ times number of depths. Lastly, the inverse STFT has a computational complexity of $\mathcal{O}(r + qr \log q)$.²² In summary, when implementing ADMIRE beamforming, the additional computational cost beyond normal DAS beamforming is $\mathcal{O}[r + r(u^3 + u^2v)w + ru + pqr \log q + qr \log q]$, where w is the number of frequencies used in the model decomposition.

2.4 Image Quality Assessment

To evaluate ADMIRE's performance, we selected images formed from 1 plane wave and multiple steered plane waves (3, 11, 31, and 75).²³ We compare results using image quality metrics for anechoic cyst phantom images derived from DAS and ADMIRE. We measured contrast and contrast-to-noise ratio (CNR) using

$$C = -20 \log_{10} \left(\frac{\mu_L}{\mu_B} \right), \quad (9)$$

$$CNR = 20 \log_{10} \left(\frac{|\mu_L - \mu_B|}{\sqrt{\sigma_L^2 + \sigma_B^2}} \right), \quad (10)$$

where (μ_L, σ_L^2) and (μ_B, σ_B^2) denote the values of the mean and variance of the enveloped but uncompressed image inside and outside the anechoic structures, respectively. These metrics differ from those chosen by the PICMUS challenge committee.^{14,15} We also compared the point spread functions of resolution target phantoms reconstructed from 1 and 75 steered plane waves, along with linear scan cases having 3 or 4 cm transmit foci. (Note that 75 steered plane waves represent the full set of plane waves acquired.) The linear scan data were not part of the PICMUS challenge. Each set of point spread functions were created using DAS with rectangular window, DAS with Hann apodization, ADMIRE with rectangular window, and ADMIRE with Hann apodization on receive.

Apart from the above, it is worth noting that the processing in ADMIRE is nonlinear so that it is important to evaluate two different sequences—(i) processing synthetic aperture first, and then applying ADMIRE and (ii) the application of ADMIRE followed by SAF. Based on this, we investigated ADMIRE images formed by both sequences. We used 3 and 11 steered plane waves with an increment of 0.43 deg. We qualitatively compared resulting images for 3 and 11 steered plane wave cases with ADMIRE, as well as SAF only (i.e., DAS). We also quantified the axially integrated power to determine which sequence may be more effective to suppress off-axis energy when applying ADMIRE.

2.5 In Vivo Evaluation

We applied ADMIRE to *in vivo* carotid artery data, which was also provided by the PICMUS competition as additional data.^{14,15} The dataset includes *in vivo* carotid artery data collected using the same parameters as shown in Table 2. Data were acquired in the cross section of a carotid artery. We used the same evaluation metrics as described in 2.4. We generated DAS B-mode images using single plane wave and multiple steered plane waves (3, 11, and 75) with SAF. We applied ADMIRE to the data to reconstruct ADMIRE B-mode images.

2.6 Evaluation with Additive Random Noise

We also investigated the effects on plane wave image quality when applying ADMIRE in the presence of uncorrelated noise. We used simulated cyst phantom data from the PICMUS using 75 steered plane waves. We then added white Gaussian noise to the channel data with signal-to-noise ratio (SNR) between -20 dB and 60 dB with an increment of 10 dB SNR. We reconstructed B-mode images after applying DAS and ADMIRE, respectively, to compute contrast and CNR using Eqs. (7) and (8), respectively.

2.7 Proposed Envelope Detection Method

In evaluating post-ADMIRE decluttered signals, we identified limitations associated with the conventional envelope detection method based on the Hilbert transform. In order to minimize the limitations, we implemented envelope detection using an optimum equiripple finite impulse response (FIR) Hilbert filter

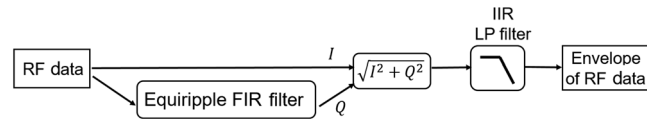


Fig. 1 The block diagram of the proposed envelope detection method, referred to as the FIR Hilbert filter, to fully realize the benefits obtained from using ADMIRE.

based on the Parks–McClellan algorithm^{27,28} followed by a fifth-order low-pass Butterworth filter (i.e., IIR LP filter). We examined the effect of using the FIR Hilbert envelope detection when applying DAS and ADMIRE in the presence of various levels of added random noise. Figure 1 shows the block diagram of the proposed envelope detection method, which is referred to as FIR Hilbert filter.

2.8 Speckle Signal-to-Noise Ratio Measurements

Finally, we compare speckle patterns obtained from ADMIRE to focused and unfocused plane wave sequences. To test this, we simulated and compared a simulated homogeneous phantom with sufficient scatterer density to ensure fully developed speckle.²⁹ We used Field II simulation¹⁷ with parameters indicated in Table 1. In the first case, conventional transmit beam sequences with focal depth of 5 cm were used, whereas the second case used unfocused beam sequences with 75 steered plane waves synthetically combined. We then applied ADMIRE to each of these two sets of speckle data. Finally, we measured the speckle (SNR_{speckle}) of each case as a function of depth, using

$$SNR_{\text{speckle}} = \frac{\mu_B}{\sigma_B}, \quad (11)$$

where (μ_B, σ_B^2) are the same denotations in Eqs. (9) and (10). When computing the values of SNR_{speckle} , rectangular kernels were applied with 5 mm height and 25 mm width with 98% overlap.

3 Results

Figure 2 demonstrates two sets of different phantom images reconstructed after applying ADMIRE. The first set of results was generated with parameters tuned for focused transmit beams but applied to plane wave sequences, whereas the second set is with parameters tuned specifically for a single plane wave image sequence. Comparing the two sets of ADMIRE images using different tuning parameters, it is apparent that optimally tuned parameters for a specific sequence substantially impact ADMIRE performance in recovering and improving image quality while preserving speckle statistics.

Figure 3 shows B-mode images of contrast cyst phantoms after applying DAS and ADMIRE beamforming, obtained from 1, 11, and 75 steered plane waves. The 11 and 75 plane wave images were formed after SAF followed by DAS and ADMIRE. The results of contrast and CNR measurements for these cases (simulated and tissue-mimicking cyst phantoms) including 1, 3, 11, 31, and 75 steered plane waves are plotted as a function of number of steered plane waves in Fig. 4. The results of the ADMIRE algorithm are based on parameters tuned for plane wave transmit sequences. These findings suggest that ADMIRE provides a boost to plane wave image quality compared with conventional DAS beamforming. It is also noticeable that improvements in contrast and CNR increase until the number

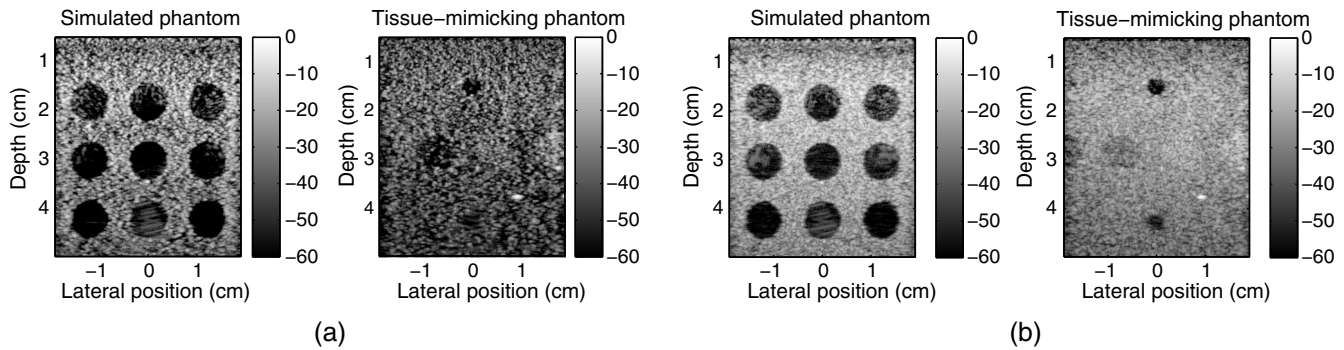


Fig. 2 Two sets of single plane wave B-mode images of cyst phantoms [simulated (left), tissue-mimicking (right)], obtained from ADMIRE with (a) previously tuned parameters for focused transmit beam sequences and (b) tuning specifically for plane wave imaging.

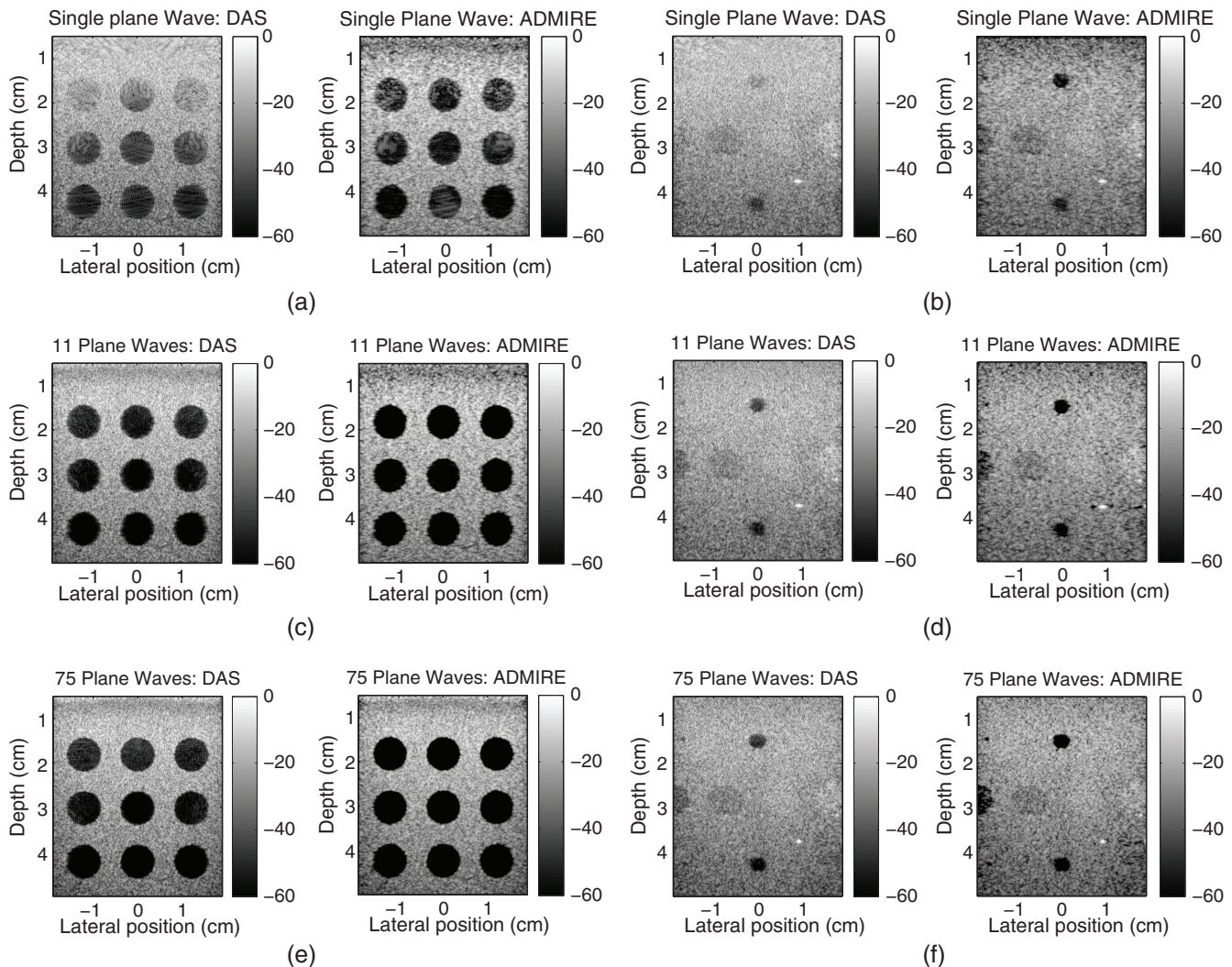


Fig. 3 Plane wave images formed after applying DAS and ADMIRE, using simulated anechoic cyst phantom (left) and tissue-mimicking phantom (right). Sets of images: (a)–(b), (c)–(d), and (e)–(f) were formed from 1, 11, and 75 steered plane waves with SAF, respectively.

of plane waves reads 11 for both DAS and ADMIRE cases, but after 11 steered plane waves the contrast and CNR values converge.

Next, in Fig. 5, we present the outcome of ADMIRE’s performance using resolution target phantom simulations with a point target at 3-cm depth on axis. The figure includes sets

of 2-D, axially integrated 1-D lateral and 1-D axial point spread functions derived from applying DAS and ADMIRE with and without Hann apodization. The point spread functions show that ADMIRE significantly reduces side-lobes compared with DAS after applying Hann apodization while preserving the spatial resolution of DAS without apodized beams. It is also interesting

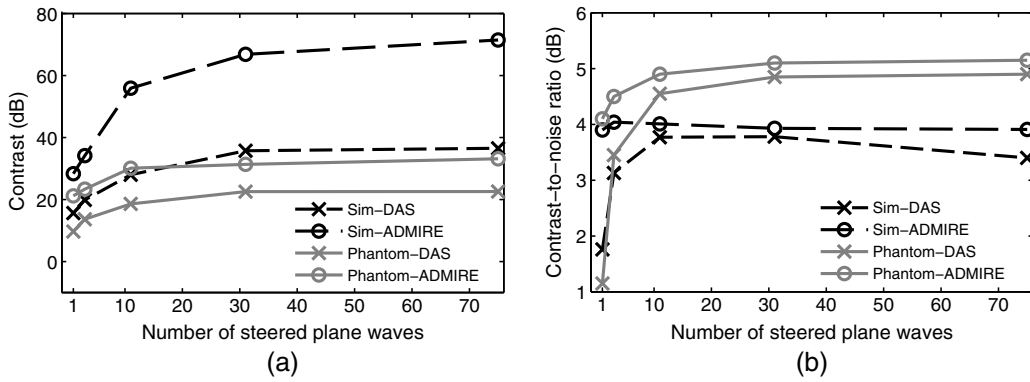


Fig. 4 Plot of (a) contrast and (b) CNR measurements for simulated and tissue-mimicking cyst phantoms as a function of number of steered plane waves. The contrast and CNR values are quantified from DAS and ADMIRE B-mode images obtained using 1, 3, 11, 31, and 75 steered plane waves.

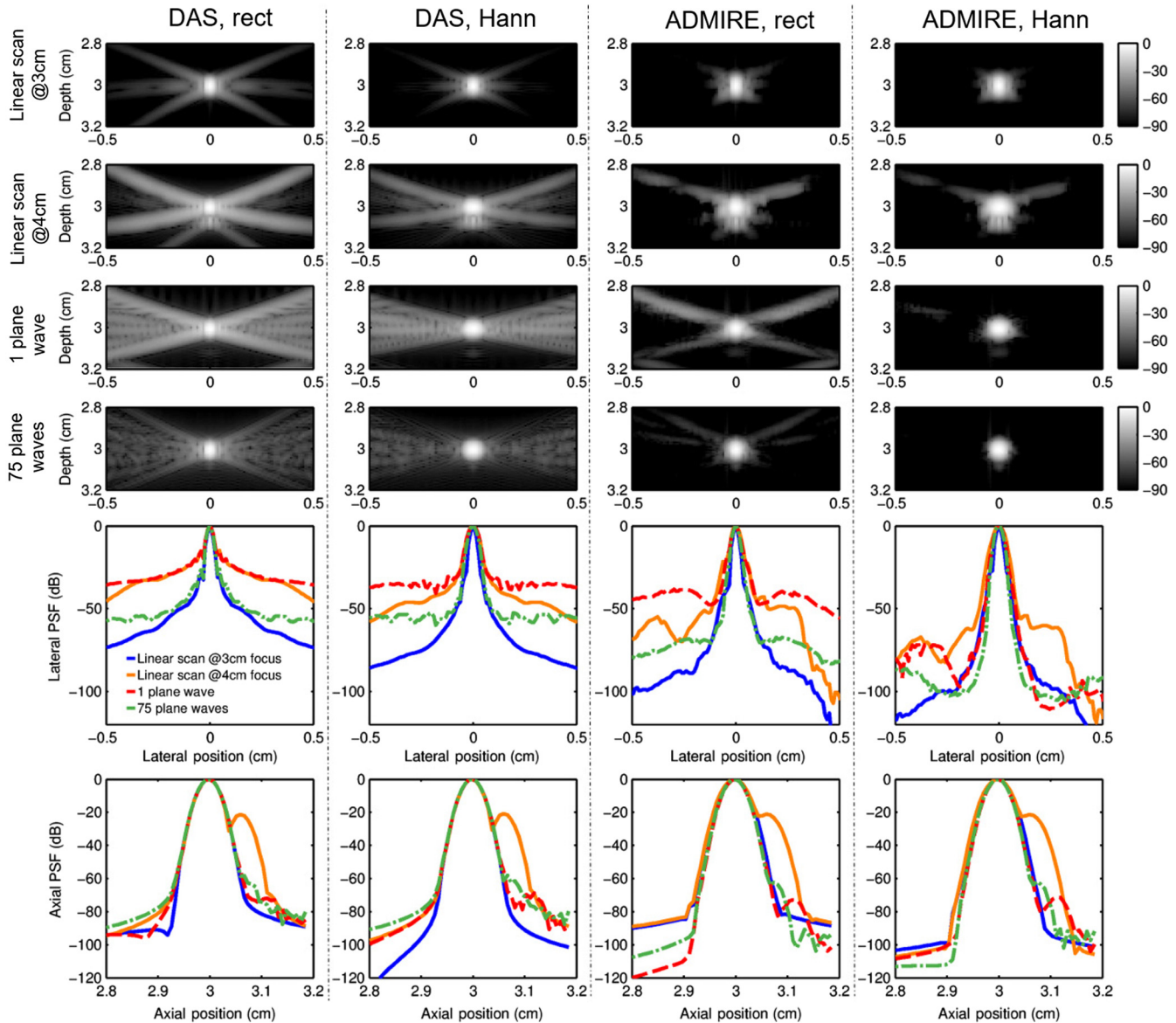


Fig. 5 ADMIRE assessment using simulated resolution phantoms with a point target 3 cm deep and on-axis, using 1 and 75 steered plane wave(s) acquisition sequences, along with linear scan acquisitions having 3 or 4 cm transmit foci. Sets of 2-D and axially integrated 1-D lateral and 1-D axial point spread functions are demonstrated. Each set of point spread functions was simulated after applying DAS with rectangular window, DAS with Hann apodization, ADMIRE with rectangular window, and ADMIRE with Hann apodization.

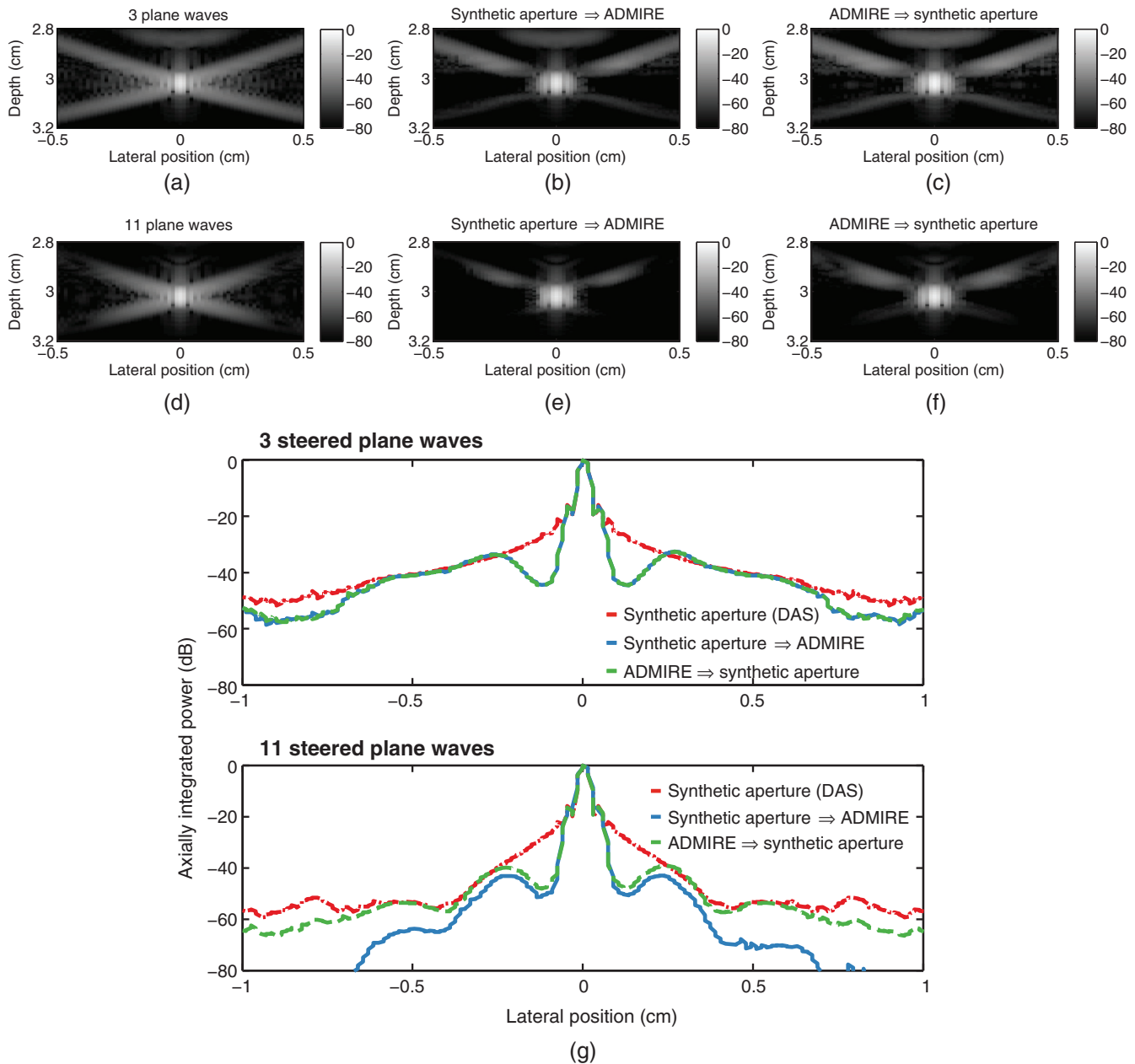


Fig. 6 Simulated resolution phantom images obtained from 3 and 11 steered plane waves applying SAF (DAS), and ADMIRE images with two different sequences: (a) and (d) DAS B-mode images formed after synthetic aperture, (b) and (e) ADMIRE B-mode images obtained with synthetic aperture to ADMIRE sequence, (c) and (f) ADMIRE B-mode images derived from applying ADMIRE followed by synthetic focusing. The corresponding lateral beam (i.e., axially integrated power) profiles are demonstrated for two sets of plane wave acquisition in (g).

to note that Hann apodization after ADMIRE provides further side-lobe reduction; although, this also results in the expected loss of lateral resolution. Note that post-ADMIRE reconstructed images and lateral beam profiles show asymmetries due to the fact that the model matrix, X in Eq. (3), used in these cases was not constructed symmetrically.

Figure 6 illustrates resolution phantom images obtained from 3 and 11 steered plane waves with SAF and ADMIRE images formed by two different sequences, along with lateral beam (i.e., axially integrated power) profiles for each case. The results suggest that despite the nonlinear aspect of ADMIRE there is little difference from the order of operation for three steered plane

waves. In using 11 steered plane waves, however, the application of ADMIRE after synthetic aperture processing is more beneficial than use of ADMIRE before synthetic aperture processing, as shown in Fig. 6(g).

Figure 7 provides *in vivo* carotid artery plane wave images derived from using DAS (top) and ADMIRE (bottom). Images were formed using 1, 3, 11, and 75 steered plane waves. When compared with DAS and ADMIRE B-mode images, we observe qualitative improvements with ADMIRE based on improved anatomical detail. We also evaluated the resulting *in vivo* images quantitatively, using image quality metrics. Table 4 shows the results of contrast and CNR measured from the *in vivo* B-mode

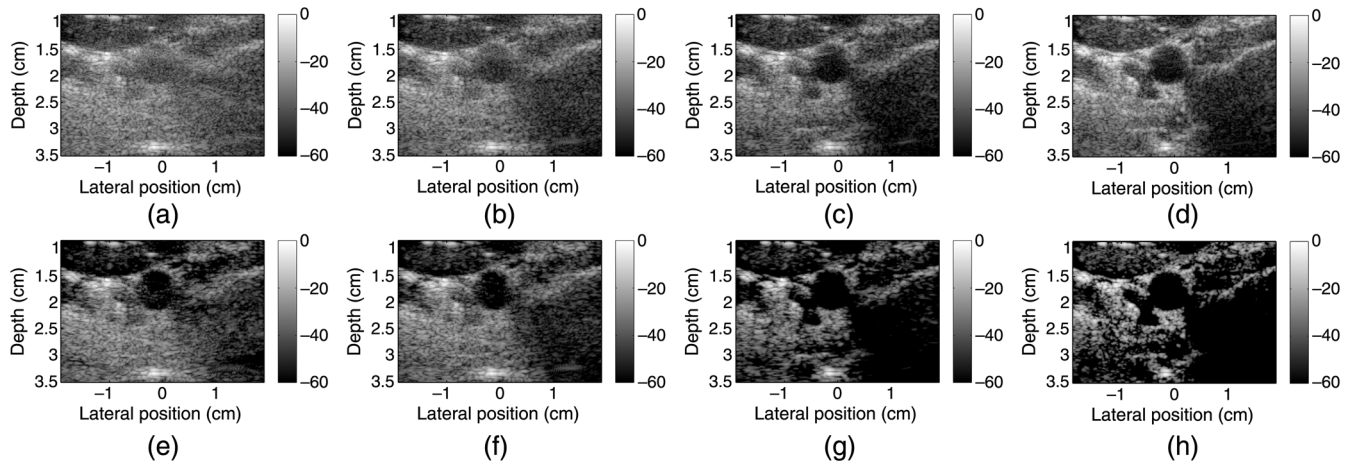


Fig. 7 *In vivo* carotid artery cross-sectional images are demonstrated. The images were obtained from 1, 3, 11, and 75 steered plane waves from left to right. The images on top (a)–(d) were formed from SAF only (DAS), whereas the images below (e)–(h) were derived using ADMIRE after SAF.

data, indicating consistency of qualitative measures in Fig. 7. Although, for the high plane wave count sets the CNR drops for both ADMIRE and DAS. Part of the challenge seems to be that it is difficult to find a uniform background region for calculating the image metrics.

Figure 8 presents B-modes images of simulated cyst phantoms with added white Gaussian noise and with varying degrees of channel data SNR between -20 and 30 dB with an increment of 10 dB SNR. The images in Fig. 8(a) were obtained from DAS, whereas the images in Fig. 8(b) were formed after applying ADMIRE. We also quantified the data using image quality metrics with additional channel data SNR of 40 , 50 , and 60 dB plus no noise in Fig. 8(c). Unsurprisingly, the results demonstrate that ADMIRE always outperforms DAS in contrast, but it is important to note that the improvements are reduced in high noise scenarios. For example, with an SNR -20 dB, the improvements are at least 10 dB higher in contrast but with an SNR 10 dB or greater the improvements are over 30 dB in contrast. It can thus be suggested that the improvement gained from applying ADMIRE is better with low noise. There is no substantial improvement in CNR when applying ADMIRE over the range of SNR. It is interesting to note that neither method approaches the theoretical limit of CNR in the presence of fully developed speckle, which is 5.6 dB.

Because we identified limitations associated with the conventional software envelope detection method using the Hilbert transform, we implemented and evaluated our proposed envelope detection method using an FIR Hilbert filter. We also investigated whether the proposed envelope detector impacts the outcome of standard DAS. Figure 9 demonstrates three sets of

results obtained from applying ADMIRE with no noise, also from DAS and ADMIRE in the presence of uncorrelated noise with an SNR of 30 dB. Each set of results includes comparisons of (1) envelope data using the conventional and proposed envelope detection methods, along with RF data and (2) B-mode images using each envelope detector.

In the ADMIRE with and without noise scenario, the enveloped signals (i.e., the red Hilbert transform lines) in Figs. 9(a) and 9(b) show much greater amplitude than the actual amplitude of the decluttered RF signals (i.e., the blue lines), degrading image contrast after the log-compression. These findings indicate that decluttered RF signals derived from ADMIRE are degraded by the postprocessing of image formation. We observe better image contrast using the proposed method in Figs. 9(g) and 9(h), compared with the images processed by the conventional method in Figs. 9(d) and 9(e). The DAS case with channel SNR 30 dB did not indicate the limitation in Fig. 9(f), in comparison with Fig. 9(i).

Quantitatively, we measured the contrast and CNR with respect to channel SNR, as shown in Fig. 10. The improvement from applying our proposed FIR filter envelope detector to post-ADMIRE decluttered signals was 7 dB in contrast when the channel data SNR is at least 30 dB or higher. There is no improvement for below 20 dB SNRs. The FIR-based envelope detector did not provide any improvement at any SNR when using DAS beamforming. Based on these findings, our proposed envelope detector enables us to fully realize the benefits obtained from the ADMIRE algorithm.

Figure 11 presents two reconstructed speckle patterns after applying ADMIRE, each of which was simulated using Field II

Table 4 Results of *in vivo* contrast and CNR measurements.

Number of plane waves	1		3		11		75	
	DAS	ADMIRE	DAS	ADMIRE	DAS	ADMIRE	DAS	ADMIRE
Contrast [dB]	10.06	28.43	15.48	28.46	20.27	42.84	23.87	47.38
CNR [dB]	-0.51	2.02	0.60	1.60	0.61	0.10	-1.39	-2.73

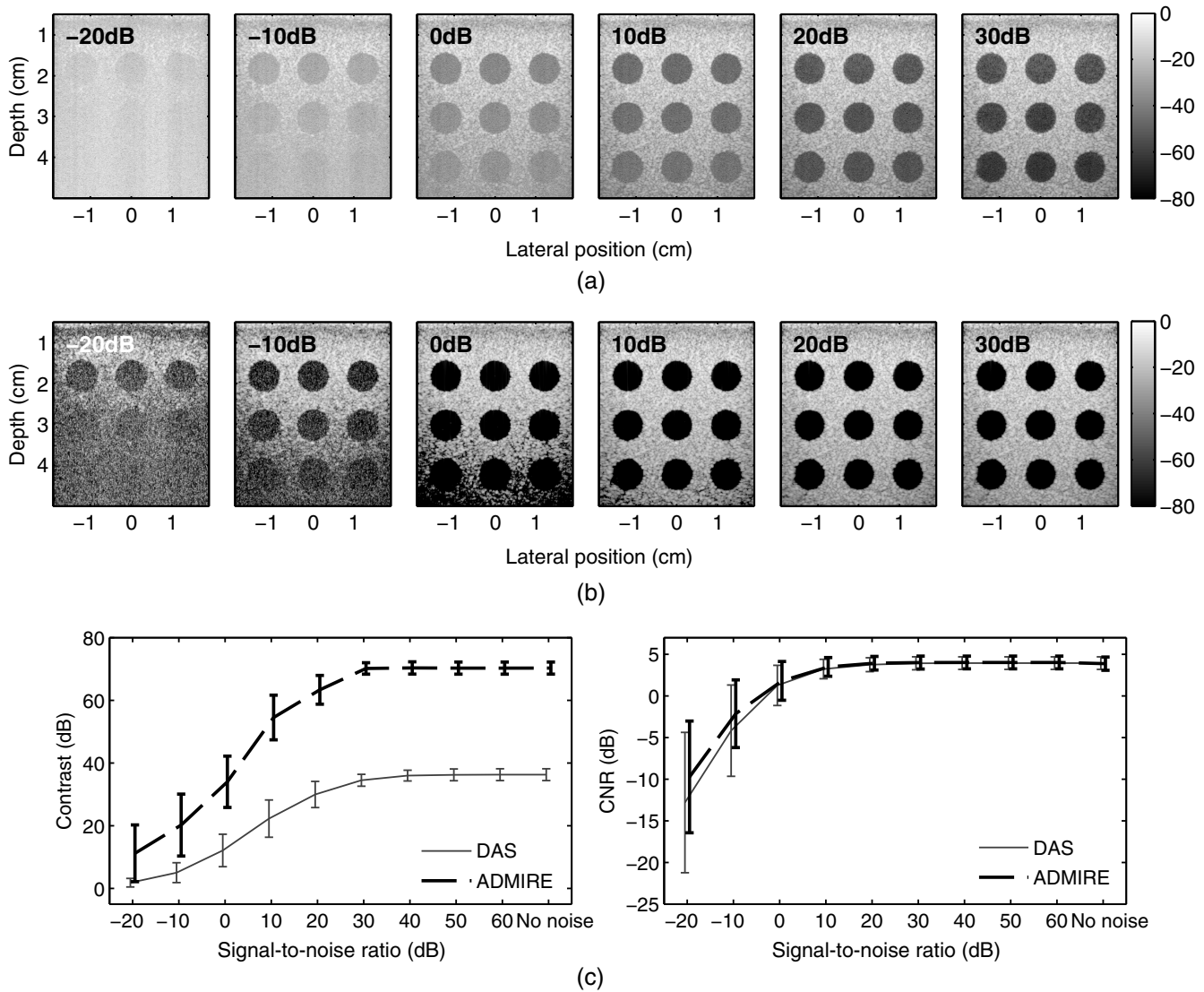


Fig. 8 B-modes images of simulated cyst phantoms with added white Gaussian noise with channel data SNR between -20 and 30 dB with an increment of 10 dB SNR, quantified using image quality metrics with additional channel SNR 40 , 50 , and 60 dB plus no noise case. The reconstructed images were obtained from (a) DAS and (b) ADMIRE, along with contrast and contrast-to-noise (CNR) as a function of channel SNRs in (c).

simulation in (a) a focused transmit beam sequence at 5 cm depth and (b) unfocused transmit beam sequences using 75 angled plane waves followed by SAF. It is interesting to note that the focused case shows that speckle texture is well recovered at a focal depth of 5 cm, but speckle patterns in the near- and far-fields were distorted. In contrast, the use of plane wave sequencing with SAF provides a uniformly distributed speckle texture reconstructed after the application of ADMIRE. As a quantitative measure, the speckle SNR in Eq. (11) was computed with respect to depth in Fig. 10(c), indicating that ADMIRE has the ability to preserve the first-order speckle statistics ($=1.91$) over the depth of field when applied to plane wave imaging with multiple acquisition angles.^{30,31} However, ADMIRE speckle patterns obtained from focused transmit beam sequences show only high speckle SNR at and near the focal depth, whereas DAS provides high speckle SNR through the depth of field.

4 Discussion

Referring to the results in Fig. 4, the contrast improvements in images obtained from single and multiple steered plane waves with and without applying ADMIRE are improved by nearly a factor of 2 on a dB scale in the case of simulated cyst phantoms, whereas the tissue-mimicking phantom cases have over 10 dB improvement in contrast after the application of ADMIRE. In comparing CNR values, ADMIRE may provide more relative benefit when applied to images obtained using single plane waves or fewer steered plane waves. As demonstrated in Fig. 7, we also observed both qualitative and quantitative improvements in *in vivo* images. The findings indicate that ADMIRE improves images generated from plane wave sequences even beyond the benefits realized by synthetic aperture processing alone.

In Fig. 2, we demonstrated that ADMIRE must be tuned appropriately to accommodate the additional clutter encountered in plane wave sequences. It is worth noting that the results of

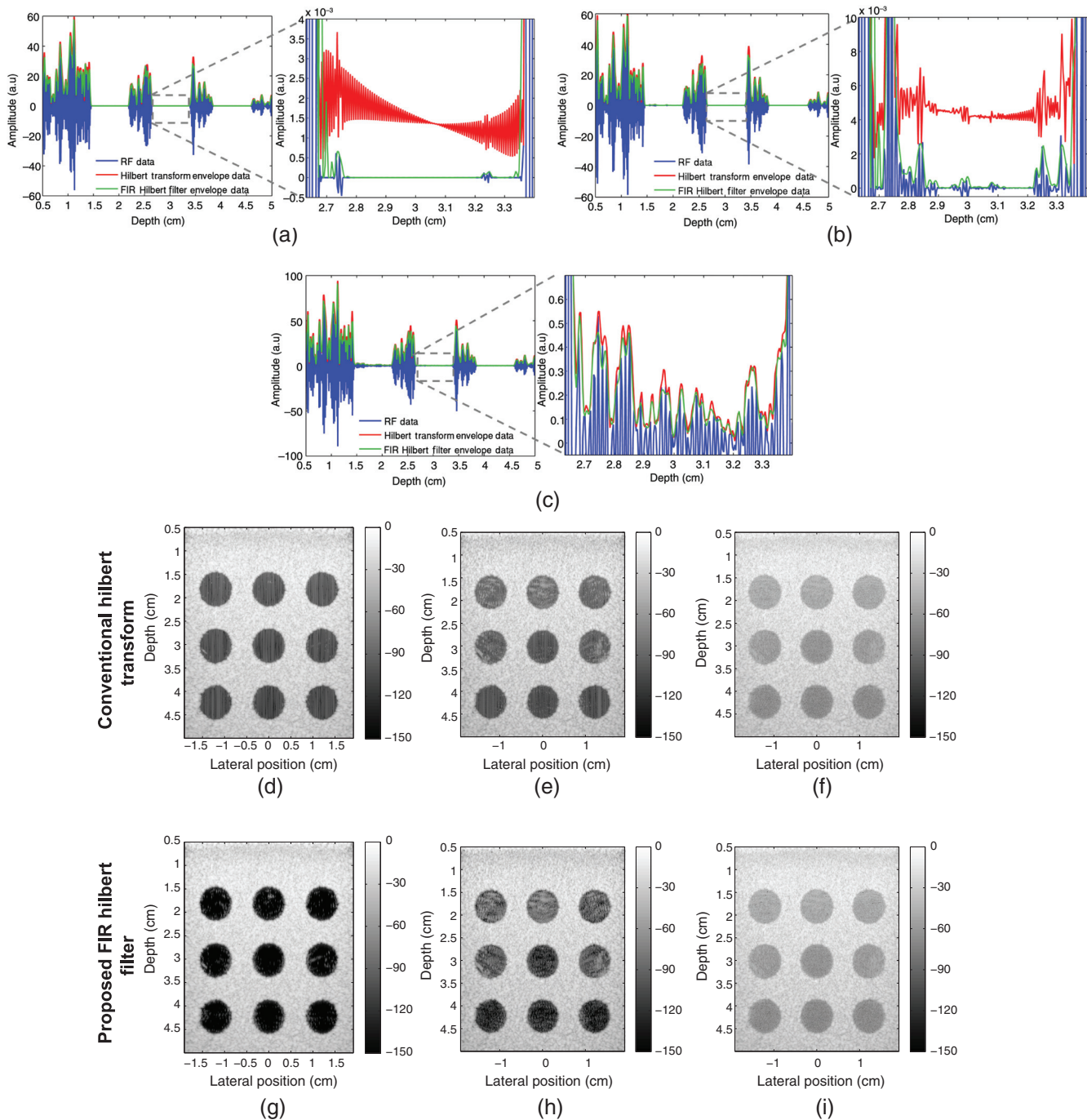


Fig. 9 Simulated cyst phantom data reconstructed from ADMIRE with and without noise, followed using a conventional (Hilbert transform) and the proposed (FIR Hilbert filter) envelope detection methods, along with the matched DAS with noise. The added noise level is channel SNR 30 dB. Both methods are compared using (1) enveloped data along with RF data, (2) B-mode images that have been processed by the conventional Hilbert transform and the proposed FIR Hilbert filter envelope detectors. (a), (d) and (g) are ADMIRE, no noise; (b), (e) and (h) are ADMIRE, SNR 30 dB; and (c), (f) and (i) are DAS, SNR 30 dB cases. (Note that we filtered out the low-frequency information that can cause Hilbert transform artifacts before applying both methods.)

the *in vivo* cases may improve when applying ADMIRE with a model space that also accounts for reverberation clutter. This should be considered in future work.

Using the same simulated cyst phantom data, we also investigated the impact of thermal noise (i.e., white Gaussian noise) on ADMIRE model decomposition and reconstruction. The results in Fig. 8 show that ADMIRE outperforms DAS.

In Figs. 9 and 10, we showed that for at least some simulations with and without random noise, ADMIRE induced improvements exceed the limitations of the conventional software Hilbert transform-based envelope detector. But, as demonstrated in Figs. 9(f) and 9(i), the DAS cases using a conventional and the proposed envelope detection methods do not show any difference. These findings suggest that other envelope detection

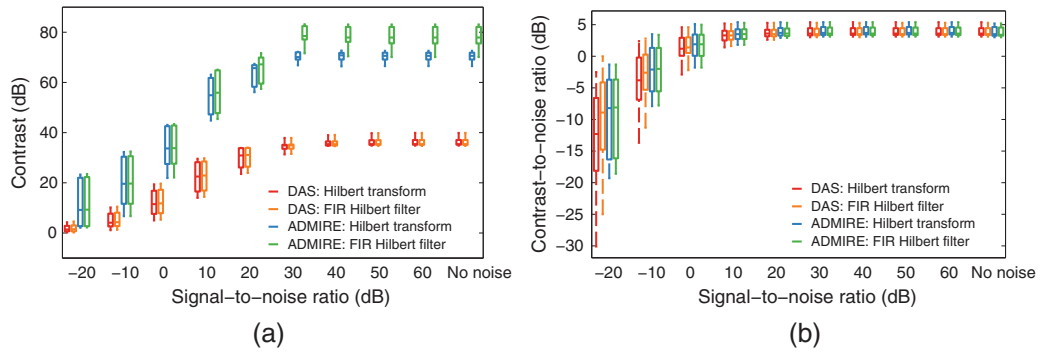


Fig. 10 Image quality metrics with respect to SNR along with no noise of DAS and ADMIRE B-mode images processed by the conventional Hilbert transform and the proposed FIR Hilbert filter envelope detectors. (a) contrast and (b) CNR.

algorithms may be required to fully realize the benefits provided by ADMIRE or other advanced beamformers.

One major concern with respect to ADMIRE is its lengthy run-time due to its high computational complexity. The ADMIRE algorithm is “embarrassingly” parallel so GPUs or

multicore CPUs will speed up performance. There are several potential approaches in related literature, such as support vector machine-based elastic-net regularization³² and beamforming using deep neural networks³³ that may also speed up ADMIRE.

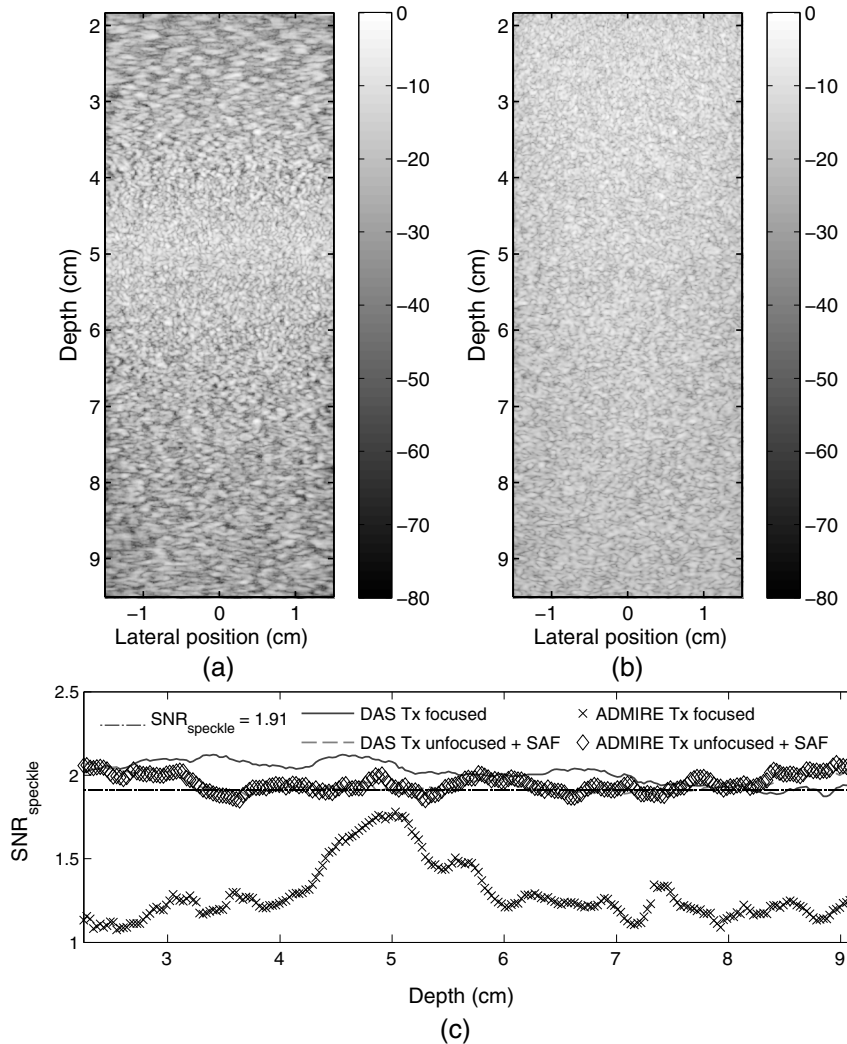


Fig. 11 Post-ADMIRE reconstructed uniform speckles in (a) a focused transmit (Tx) beam sequence at 5-cm depth, (b) an unfocused transmit beam sequence with 75 steered angles, which are summed to synthesize transmit aperture focusing at all depths (i.e., plane wave sequence of 75 angles with an increment of 0.43 deg, using SAF). The speckle (SNR_{speckle}) are measured and plotted as a function of depth for each acquisition in (c).

Finally, the results in Fig. 11 indicate that adaptive tuning would be necessary to preserve the speckle in other regions outside the focal depth of field, but this is not necessary when using synthetic aperture techniques. Ultimately, these findings suggest that ADMIRE performance and its outcome rely not only on selection of the tuning parameters but also on the acquisition sequence.

5 Conclusions

In this study, we demonstrated that ADMIRE can be adapted to full-field insonification sequences. We specifically showed this using plane wave transmit sequences with and without SAF. ADMIRE also shows an ability to suppress random white noise to provide a boost in thermal SNR. Finally, we demonstrated that in some cases a further improvement can be achieved using a different envelope detector.

Disclosures

No conflicts of interest, financial or otherwise, are declared by the authors.

Acknowledgments

The authors would like to thank the staff of the Vanderbilt University ACCRE computing resource. This work was supported by NIH grants R01EB020040 and S10OD016216-01.

References

- P.-C. Li and M.-L. Li, "Adaptive imaging using the generalized coherence factor," *IEEE Trans. Ultrason. Ferroelectr. Freq. Control* **50**(2), 128–141 (2003).
- Q. Ma et al., "Improvement of tissue harmonic imaging using the pulse-inversion technique," *Ultrasound Med. Biol.* **31**(7), 889–894 (2005).
- I. K. Holfort, F. Gran, and J. A. Jensen, "Broadband minimum variance beamforming for ultrasound imaging," *IEEE Trans. Ultrason. Ferroelectr. Freq. Control* **56**(2), 314–325 (2009).
- M. A. Lediju et al., "Short-lag spatial coherence of backscattered echoes: imaging characteristics," *IEEE Trans. Ultrason. Ferroelectr. Freq. Control* **58**(7), 1377–1388 (2011).
- B. Byram and M. Jakovljevic, "Ultrasonic multipath and beamforming clutter reduction: a chirp model approach," *IEEE Trans. Ultrason. Ferroelectr. Freq. Control* **61**(3), 428–440 (2014).
- B. Byram et al., "A model and regularization scheme for ultrasonic beamforming clutter reduction," *IEEE Trans. Ultrason. Ferroelectr. Freq. Control* **62**(11), 1913–1927 (2015).
- K. Dei and B. Byram, "The impact of model-based clutter suppression on cluttered, aberrated wavefronts," *IEEE Trans. Ultrason. Ferroelectr. Freq. Control* **64**(10), 1450–1464 (2017).
- B. Byram, J. Shu, and K. Dei, "Nonlinear beamforming of aperture domain signals," in *IEEE Int. Ultrasonics Symp. (IUS 2015)*, pp. 1–6, IEEE (2015).
- M. Cikes et al., "Ultrafast cardiac ultrasound imaging: Technical principles, applications, and clinical benefits," *JACC: Cardiovasc. Imaging* **7**(8), 812–823 (2014).
- J. Bercoff, "Ultrafast ultrasound imaging," in *Ultrasound Imaging-Medical Applications*, InTech (2011).
- L. Tong et al., "Comparison of conventional parallel beamforming with plane wave and diverging wave imaging for cardiac applications: a simulation study," *IEEE Trans. Ultrason. Ferroelectr. Freq. Control* **59**(8), 1654–1663 (2012).
- J. Udesen et al., "High frame-rate blood vector velocity imaging using plane waves: simulations and preliminary experiments," *IEEE Trans. Ultrason. Ferroelectr. Freq. Control* **55**(8), 1729–1743 (2008).
- K. Dei, J. Tierney, and B. Byram, "Aperture domain model image reconstruction (ADMIRE) with plane wave synthesis," *Proc. SPIE* **10139**, 1013911 (2017).
- H. Liebgott et al., "Plane-wave imaging challenge in medical ultrasound," in *IEEE Int. Ultrasonics Symp. (IUS 2016)*, pp. 1–4, IEEE (2016).
- H. Liebgott et al., "Plane-wave imaging challenge in medical ultrasound (PICMUS)," in *IEEE Int. Ultrasonics Symp. (IUS 2016)*, Tours, France, https://www.creatis.insa-lyon.fr/Challenge/IEEE_IUS_2016/ (21 September 2016).
- J. A. Jensen and N. B. Svendsen, "Calculation of pressure fields from arbitrarily shaped, apodized, and excited ultrasound transducers," *IEEE Trans. Ultrason. Ferroelectr. Freq. Contr.* **39**(2), 262–267 (1992).
- J. A. Jensen, "Field: a program for simulating ultrasound systems," in *10th Nordic-Baltic Conf. on Biomedical Imaging*, Vol. 4, pp. 351–353 (1996).
- A. Selfridge, G. Kino, and B. Khuri-Yakub, "A theory for the radiation pattern of a narrow-strip acoustic transducer," *Appl. Phys. Lett.* **37**(1), 35–36 (1980).
- J. Friedman, T. Hastie, and R. Tibshirani, "Regularization paths for generalized linear models via coordinate descent," *J. Stat. Software* **33**(1), 1 (2010).
- H. Zou and T. Hastie, "Regularization and variable selection via the elastic net," *J. R. Stat. Soc. B* **67**(2), 301–320 (2005).
- R. J. Tibshirani et al., "Degrees of freedom in lasso problems," *Ann. Stat.* **40**(2), 1198–1232 (2012).
- B. Yang, "A study of inverse short-time Fourier transform," in *IEEE Int. Conf. on Acoustics, Speech and Signal Processing*, pp. 3541–3544 (2008).
- G. Montaldo et al., "Coherent plane-wave compounding for very high frame rate ultrasonography and transient elastography," *IEEE Trans. Ultrason. Ferroelectr. Freq. Control* **56**(3), 489–506 (2009).
- J. T. Ylitalo and H. Ermert, "Ultrasound synthetic aperture imaging: monostatic approach," *IEEE Trans. Ultrason. Ferroelectr. Freq. Control* **41**(3), 333–339 (1994).
- J. A. Jensen et al., "Synthetic aperture ultrasound imaging," *Ultrasonics* **44**, e5–e15 (2006).
- R. S. Cobbold, *Foundations of Biomedical Ultrasound*, Oxford University Press (2007).
- D. E. T. Romero and G. J. Dolecek, *Digital FIR Hilbert Transformers: Fundamentals and Efficient Design Methods*, INTECH Open Access Publisher (2012).
- M. A. Hassan and Y. M. Kadah, "Digital signal processing methodologies for conventional digital medical ultrasound imaging system," *Am. J. Biomed. Eng.* **3**(1), 14–30 (2013).
- R. F. Wagner et al., "Statistics of speckle in ultrasound b-scans," *IEEE Trans. Sonics Ultrason.* **30**(3), 156–163 (1983).
- C. B. Burckhardt, "Speckle in ultrasound b-mode scans," *IEEE Trans. Sonics Ultrason.* **25**(1), 1–6 (1978).
- M. E. Anderson and G. E. Trahey, *A Seminar on k-Space Applied to Medical Ultrasound*, Department of Biomedical Engineering, Duke University (2000).
- Q. Zhou et al., "A reduction of the elastic net to support vector machines with an application to GPU computing," in *Proc. of the Twenty-Ninth AAAI Conf. on Artificial Intelligence*, pp. 3210–3216 (2015).
- A. C. Luchies and B. C. Byram, "Deep neural networks for ultrasound beamforming," *IEEE Trans. Med. Imaging* (2018).

Kazuyuki Dei received his BS degree in mechanical engineering from the University of California, Berkeley, CA, in 2000. He is a graduate student pursuing a PhD degree in biomedical engineering at Vanderbilt University, Nashville, TN, USA. His research interests include model-based clutter suppression, phase-aberration measurements, beamforming, and signal processing.

Jaime Tierney received her BA degree in mathematics in 2012 from the College of the Holy Cross in Worcester, MA. She is also a graduate student pursuing a PhD degree in biomedical engineering at Vanderbilt University, Nashville, TN, USA. Her research interests include microvasculature perfusion estimation techniques using non-contrast ultrasound imaging.

Brett Byram received his BS degree in biomedical engineering and mathematics from Vanderbilt University and his PhD in biomedical engineering from Duke University in 2011. He is an assistant professor at the Vanderbilt University School of Engineering. He is affiliated with the Vanderbilt Institute in Surgery and Engineering (VISE) and the Vanderbilt University Institute of Imaging Science. He is a member of SPIE.